Available online at www.CivileJournal.org

Civil Engineering Journal

(E-ISSN: 2476-3055; ISSN: 2676-6957)

Vol. 11, No. 07, July, 2025

Response of Long-term Cyclic Laterally Loaded Monopiles in Sand

M. M. Khalaf [1*], Rami M. El-Sherbeiny [2], Ahmed M. Ebid [1], Shehab S. Agaiby [2]

[1] *Future University, Cairo, Egypt.*

[2] *Faculty of Engineering, Cairo University, Giza 12311, Egypt.*

Received 30 January 2025; Revised 19 June 2025; Accepted 24 June 2025; Published 01 July 2025

Abstract

The offshore wind energy industry has grown rapidly, with large-diameter monopiles becoming the primary foundation choice for offshore turbines. Monopile designs emphasize serviceability and fatigue limits, enforcing strict rotation limits set by manufacturers. These structures face considerable lateral cyclic loads from waves, currents, and wind. Existing design codes such as API and DNV GL are commonly used but do not sufficiently capture monopile behavior under cyclic loading, particularly regarding load cycle count, amplitude, and type. Moreover, the dynamic response of the monopile-soil system, which affects the foundation's natural frequency, depends on the pile-soil interaction stiffness—an aspect neglected in current standards. This research reports results from seventeen 1-g cyclic loading experiments and six monotonic tests on monopiles installed in dry sand. Findings reveal that cyclic deformation is significantly influenced by sand relative density, load cycle number, and cyclic load characteristics (magnitude and type). Cyclic loading also alters the pile-soil stiffness. Accumulated rotation grows exponentially with increasing load cycles, while cyclic secant stiffness increases logarithmically. The study further identifies asymmetric two-way cyclic loading as the most damaging load pattern for monopile performance.

Keywords: Lateral Cyclic Loading; Monopile; Offshore Wind Turbines; Pile Accumulated Rotation; 1-g Test.

1. Introduction

Nowadays, vast areas around the world are suffering from the effects of climate change. So, governments must use renewable energy to reduce carbon dioxide emissions. Wind energy is a promising solution for climate change problems due to its low impact on the environment, cost efficiency, and sustainability. The contribution of wind energy increased significantly in this decade by a 9% year-on-year growth. In 2022, 77.6 GW of wind power was added to the power grids all around the world [1].

Onshore and offshore wind turbines can generate wind energy. Despite the high installation cost of offshore wind turbines, there are many advantages to offshore wind turbines, such as high utilization of wind due to the high speed of the wind, which exceeds 7 m/s and has a steadier flow compared to onshore wind turbines. Hence, the electric power produced by offshore wind energy ranges between 1.5 to 2 times the electric power generated by onshore wind turbines, which makes the use of offshore wind turbines more efficient in the long term. The added electric power by offshore wind turbines is doubled every three years, according to the global annual wind energy report, and it is expected to continue to grow at the same rate [2].

Monopile is the most preferred foundation system to support offshore wind turbines due to its sizeable lateral load capacity, durability, and easy installation. It has been used for 81% of the currently installed offshore wind turbines

* Corresponding author: mahmood.khalaf@fue.edu.eg

http://dx.doi.org/10.28991/CEJ-2025-011-07-012

worldwide [3, 4]. It is a substantial open-ended steel tube with a diameter ranging from 3 to 12 m, an embedded length usually less than 50, and an aspect ratio (L/D) ranging between 3 and 8. It is often used in relatively shallow water depths ranging from 20 to 40 m, and it is driven on sand and clay seabed by impact hammers and vibratory driving. It is not clear whether it will be economical if it is used in deeper water. Over their operational lifespan, these monopiles can undergo over one million cycles of loading due to wind, wave, and ice loads, which potentially causes permanent deformation that impacts the efficiency of wind turbines [5]. Thus, precisely evaluating the behavior of monopiles under lateral cyclic loads is crucial to maintain the stable functioning of wind turbines. Moreover, monitoring installed monopiles indicates that the actual foundation stiffness is greater than the predicted stiffness by existing design methods. More accurate design methods are required to reduce the installation cost by estimating more suitable stiffness, which will reduce the weight and embedment length of monopile foundations [6]. Figure 1 represents a schematic of a typical monopile foundation system for offshore wind turbines.

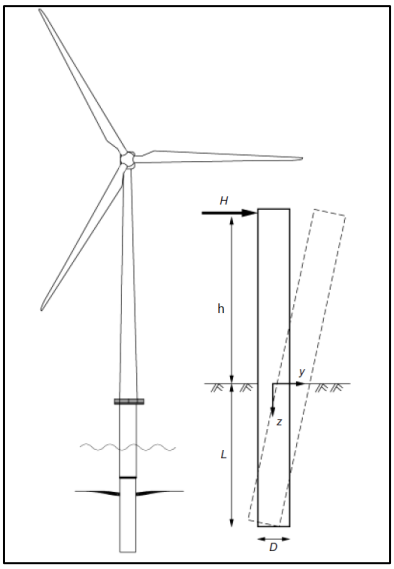

Figure 1. Typical monopile foundation system for offshore wind turbines [7]

1.1. Current Guidelines

Due to the rear of offshore wind turbine guidelines, the designers use the design approach, which has been used and developed by the oil and gas industry over many years to design offshore piles of fixed offshore platforms. This design approach is based on Winkler's theory, which models soil pile interaction using a series of uncoupled springs. These springs are characterized by a nonlinear empirical behavior correlation between lateral pile deflection and soil resistance, which is known as the p-y curve. Reese et al. a semi-empirical p-y curve based on a fully instrumented full-scale pile at Mustang Island [8]. Murchison & O'Neill [6] developed a tangent hyperbolic formula to provide better results compared to the original expressions formulated by Reese et al. The tangent hyperbolic formula, as shown in Equation 1, is adopted in API RP 2A-WSD [9] and DNVGL-ST-0126 [10] guidelines.

$$p_{(x,y)} = Ap_u \tanh\left(\frac{k.x}{Ap_u}y\right) \quad (1)$$

where A is a calibration factor and determined as follows:

$$A = \begin{cases} 3 - 0.8.\left(\frac{x}{D}\right) \geq 0.9 & \text{for static loading} \\ 0.9 & \text{for cyclic loading} \end{cases}$$

where p_u is the ultimate bedding resistance, depends on the effective unit weight $\acute{\gamma}$ and the angle of internal friction $\acute{\phi}$. API and DNV proposed Equation 2 to determine the ultimate bedding resistance:

$$p_u = \min \text{of} \begin{cases} (C_1.x + C_2.D)\acute{\gamma}x & \text{for } 0 < x < x_R \\ C_3.D.\acute{\gamma}.\ x & \text{for } x > x_R \end{cases} \quad (2)$$

where k is the initial stiffness coefficient that depends on the angle of internal friction ϕ or sand relative density and is specified from the curve presented by API as shown in Figure 1; C_1, C_2, and C_3 are dimensionless coefficients depending on the angle of internal friction as shown in Figure 2; x is soil depth y is pile lateral displacement.

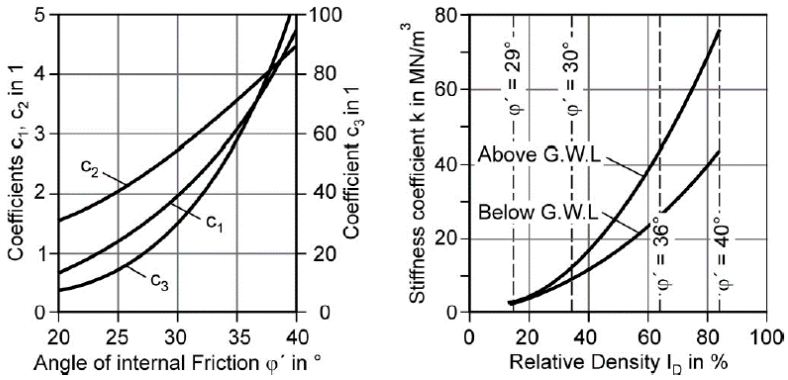

Figure 1. C_1, C_2, C_3 coefficients, and initial stiffness coefficient according to API [9]

1.2. Limitations of Current Design Methods

There are some limitations of the current design approach, as stated as follows:

- Current design p-y curve methods are based on empirical data obtained from full-scale pipe pile tests at Mustang Island, where the pile diameter is 0.61 m, wall thickness, and embedded length 21 m, which corresponds to an aspect ratio of L/D = 34.4. Therefore, the tested pile behaves as a long flexible pile while the monopile of a large diameter from 3 to 12 m and aspect ratio of L/D = 3-8, behaves as a short rigid pile. Rigid piles behave differently compared to flexible piles due to under lateral loading and moment; rigid piles rotate about a "zero kick" point without significantly flexing, as shown in Figure 1. This behaviour significantly affects the pile-soil response [11]. A criterion developed by Polous and Hull to distinguish between flexible and rigid piles relies on the relative stiffness between soil and pile and is presented in Equation 3 [12]:

$$\frac{E_s.L^4}{E_p I_p} < 4.8 \quad \text{Rigid pile}$$
$$\frac{E_s.L^4}{E_p I_p} > 388.6 \quad \text{Flexible pile} \tag{3}$$

- Current standards recommended a cyclic p-y curve by degrading the ultimate by degrading bedding resistance by 10% due to cyclic loading. So, cyclic p-y curves are obtained by using a calibration coefficient (A) equal to 0.9. This recommendation is based on full-scale tests where the pile is subjected to load cycles up to 25, while the typical offshore wind turbine is designed for fatigue with 10^7 cycles. On the other hand, this design approach does not consider essential design issues such as accumulated rotation and change of pile-soil stiffness due to long-term cyclic loading during the offshore wind turbine lifetime. According to DNVGL, the allowable rotation of offshore wind turbine rotor is 0.5°, which is divided into 0.25° due to installation effects and 0.25 due to serviceability. Therefore, the serviceability limit state (SLS) governs the design of monopiles, and accumulated rotation due to long-term cyclic design is a key design driver. Although current standards show that the pile-soil stiffness decreases due to cyclic loading, other researchers, such as Leblanc et al. [7], found that the pile-soil cyclic secant stiffness increases due to cyclic loading. Pile-soil stiffness is a primary design parameter due to modern offshore wind turbines being designed as soft-stiff structures, which means that its natural frequency ranges between the excitation frequency bands 1P and 3P to avoid resonance. 1P and 3P refer to rotor and blade passing frequencies, which are 0.3 HZ and 1 HZ, respectively. Therefore, any change in the initial stiffness of pile-soil will affect the first natural frequency, which affects the dynamic stability of offshore wind turbines [7].

- Based on a numerical calculation (3D finite element), the p-y curves recommended by API underestimate the lateral displacement of the monopile, which is subjected to lateral monotonic loading. The expected reason for these results may be an overestimation of the initial stiffness of monopiles in large depths by API. However, recent data obtained from monitoring full-scale wind turbines at Walney offshore farms demonstrate that the p-y curve adopted by API significantly underestimates the foundation stiffness [13].

- Previous researchers such as Davidson [14], Gerolymos & Gazetas [15] and Lam & Martin [16] found that further soil reactions influence monopile pile behaviour in addition to the lateral load resistance. These additional soil reactions are the vertical shear traces on the external pile surface, base moment, and horizontal base shear force. A new model known as the PISA model was developed by an academic work group lad and management at Oxford University. This model takes these additional soil reactions into account [17].

1.3. State of the Art for Predicting Pile Response due to Long-Term Lateral Cyclic Loading

Little & Briaud [18] conducted six full-scale tests and pressure meter tests to investigate factors affecting pile cyclic behavior. The results demonstrated that factors such as soil relative density, installation method, pile type, and cyclic load type significantly influence pile performance under cyclic loading. Based on these findings, the authors proposed a form to represent accumulated displacement due to cyclic loading, as shown in Equation 4, and introduced a correlation to quantify the cyclic degradation of secant stiffness, presented in Equation 5. However, it is important to note that the tested piles were subjected to a limited number of cycles, up to 25, which is relatively low compared to the actual number of cycles that typically affect monopiles. Additionally, the tested piles had a high aspect ratio (L/D) ranging from 32 to 37, while monopiles typically have an aspect ratio (L/D) ranging between 3 and 8, highlighting a key difference in the geometry of the tested piles versus typical offshore monopiles. These discrepancies suggest that further research is needed to better understand the behavior of monopiles under more realistic cyclic loading conditions.

$$y_N = y_1 . N^a \quad (4)$$

$$K_{s,N} = K_{s,1} . N^a \quad (5)$$

where Y_1 is lateral displacement determined from the monotonic response at the same cyclic amplitude, y_N is lateral displacement after N of cycles, a is cyclic degradation parameter, and its value equals 0.072 (overall average determined from the full-scale test) or 0.064 (overall average determined from pressure meter tests), $K_{s,1}$ is initial secant stiffness, $K_{s,N}$ is secant stiffness after N of cycles.

Lam & Martin [16] conducted thirty-four cyclic lateral load tests and introduced two methods to assess the effects of cyclic loading on pile behavior. The first method, the Linear Subgrade Modulus Method (LISM), employs a closed-form solution based on beam-on-elastic-foundation analysis. In this method, the subgrade modulus increases linearly with depth, as shown in Equation 6, and the coefficient of subgrade modulus degrades with the number of cycles, according to Equation 7. The second method, the Deteriorated Soil p-y Curves Method (DSPY), involves modifying the current static p-y curve to account for soil deterioration under cyclic loading, with corresponding Equations 8 and 9 for the deterioration procedure. Additionally, Equation 10 describes how the soil stiffness decreases over the number of cycles. Both methods take into account various factors affecting the cyclic loading response, such as soil density, installation method, and load type. These methodologies provide a more comprehensive framework for understanding the impact of cyclic loading on the behavior of piles, contributing valuable insights into the modeling of pile-soil interaction under repeated loading conditions.

$$K_h = n_h . z \quad (6)$$

$$n_{h,N} = n_{h,1} . N^{-t} \quad (7)$$

$$p_N = p_1 . N^{(\alpha-1)t} \quad (8)$$

$$y_N = y_1 . N^{\alpha t} \quad (9)$$

$$K_{h,N} = K_{h,1} . N^{-t} \quad (10)$$

where K_h is horizontal subgrade modulus, n_h is the horizontal coefficient of subgrade modulus, p_N is bedding resistance after N of cycles, p_1 is bedding resistance determined from static p-y curve, y_N is pile lateral displacement after N of cycles, y_1 is lateral displacement determined from static p-y curve, $K_{h,N}$ is horizontal subgrade reaction modulus after N of cycles, $K_{h,1}$ is horizontal subgrade reaction modulus determined by static p-y curve, α is a parameter to control relative contribution between soil resistance and deflection to decrease the soil modulus, and t is a cyclic degradation parameter that function of load type, installation method, and soil density as presented in Equation 11.

$$t = 0.17 \times F_L . F_I . F_D \quad (11)$$

where F_L, F_I, and F_D, are factors based on details of the cyclic load ratio, pile installation, and soil density, respectively.

Byrne et al. [17] proposed an empirical method to predict lateral accumulated strain due to cyclic loading, based on data from twenty full-scale cyclic tests. The model identifies key factors influencing cyclic loading, including soil density, installation method, cyclic load type, and pile-soil relative stiffness. To estimate the accumulated lateral strain under variable amplitude cyclic loading, the authors employed the superposition method. The model showed good agreement when calibrated with data from six additional full-scale tests. However, caution is advised when using this model to predict the effects of cyclic loading on monopiles, as the parameters were derived from cyclic loading tests with a maximum of 50 cycles. These parameters may not fully represent the long-term behaviour of monopiles under repeated loading. The proposed accumulated strain model is presented in Equation 12, which captures the relationship between cyclic loading and accumulated lateral strain, though its application should be limited to conditions similar to those of the tests conducted.

$$R_s = \frac{\varepsilon_N}{\varepsilon_1} = 1 + t \ln N \quad (12)$$

where R_s is accumulated strain due to cyclic loading, ε_1 is strain after the first cycle or obtained from monotonic loading at the same cyclic amplitude, ε_N is strain after N of cycles, N is a number of cycles, and t is cyclic degradation parameter that function of all the before mentioned factors affecting cyclic loading and determined by Equation 13.

$$t = 0.032 \times \frac{L}{T} \times \beta \times \xi \times \phi \quad (13)$$

where L is pile embedment length, and T is pile-soil relative stiffness, which equals $\sqrt[5]{\frac{EI}{n_h}}$, β is the soil density factor, ξ is the pile installation factor, and Φ is the cyclic load type factor.

Little & Briaud [18] developed a numerical model based on explicit analysis to estimate accumulated displacement due to cyclic loading. Known as the Stiffness Degradation Model (SDM), this model accounts for the effects of cyclic loading by degrading the soil's secant stiffness. The authors adapted Hurman's cyclic stiffness degradation formula, initially used to estimate plastic axial strain in cyclic triaxial tests, to include anisotropy in initial stress conditions and changes in principal stress directions after load application. This formula, as presented in Equation 14, can be incorporated into a finite element method (FEM) subroutine to deteriorate soil secant stiffness over successive cycles, enabling the calculation of accumulated displacement resulting from this stiffness degradation. The model showed strong agreement with existing experimental results. However, it does not take into account factors such as pile installation methods or cyclic load types. Additionally, Little & Briaud [18] demonstrated that the "zero-toe-kick" or "vertical tangent" criteria, commonly used in offshore wind turbine design guidelines to determine pile embedment length, are not appropriate for large-diameter monopiles, highlighting the need for revised criteria to better represent monopile behaviour.

$$\frac{E_{sN}}{E_{s1}} = \frac{\varepsilon_{cp,N=1}}{\varepsilon_{cp,N}} = N^{-b_1 (X_c)^{b_2}} \quad (14)$$

where E_{s1} is secant stiffness after the first cycle, E_{SN} is secant stiffness after N of cycles, $\varepsilon_{cp,N} = 1$ is axial plastic strain after the first cycle, $\varepsilon_{cp,N}$ is axial plastic strain after N of cycles, b_1, and b_2 are material regression parameters that determined from drained cyclic triaxial tests(For medium dens sand b_1 =0.16, b_2= 0.38 and for dense sand b_1= 0.2, b_2= 5.76), X_c is cyclic stress ratio and determined according to Equation 15.

$$X_c = \frac{X^1 - X^0}{1 - X^0}$$
$$X^0 = \frac{\sigma_1^0}{\sigma_{1f}^0}, \quad (15)$$
$$X^1 = \frac{\sigma_1^1}{\sigma_{1f}^1}$$

where, σ_1^0 is major principal stress at initial stress condition (zero loading condition), σ_{1f}^0 is major principal stress at static failure state of initial stress condition, σ_1^1 is a major principal stress after applying the first load cycle and σ_{1f}^1 is major principal stress at static failure state after applying the first load cycle.

Leblanc et al. [7] developed a non-dimensional framework and conducted a series of 1-g experimental tests to predict the behaviour of monopiles subjected to cyclic lateral loading. From these tests, they presented an exponential formula to predict the accumulated rotation of monopiles due to cyclic loading and a logarithmic function to estimate changes in soil cyclic secant stiffness. While the API guidelines suggest that soil stiffness degrades by 10% due to cyclic loading, their test results indicated that, contrary to this recommendation, soil stiffness actually increases logarithmically with the number of load cycles. The model parameters, including soil density, cyclic load amplitude, and load type (one-way or two-way), were found to be critical in influencing the results. Notably, the type of cyclic load had a significant impact on the results; it was observed that the accumulated rotation induced by asymmetric two-way loading (ζ_c = -0.6) was four times larger than that induced by one-way cyclic loading (ζ_c = 0). Equations 16 and 17 illustrate the relationship between accumulated rotation and the change in cyclic secant stiffness due to cyclic loading, providing valuable insights for modelling monopile behaviour under real-world loading conditions

$$\frac{\Delta\theta}{\theta_S} = T_b(\zeta_b, D_r).\ T_c(\zeta_c).\ N^{\alpha} \quad (16)$$

$$\tilde{k} = \tilde{k}_0 + A_k\, ln(N) \quad (17)$$

where T_b is a nondimensional parameter, the function of cyclic load magnitude (ζ_b) and soil relative density, T_c is a nondimensional parameter, a function of cyclic load type (ζ_c). Figure 3 shows curves of T_b and T_c as presented by Leblanc et al. [7], α is an accumulation coefficient with a constant value of 0.31, $\tilde{k}_0$ is nondimensional initial cyclic secant stiffness and function of dimensionless functions K_b, K_C as presented in Equation 18, and A_k is a nondimensional constant and equals 8.02.

$$\begin{aligned} \bar{k}_0 &= K_b(\zeta_b)K_C(\zeta_C) \\ \zeta_b &= \frac{M_{max}}{M_R} \\ \zeta_C &= \frac{M_{min}}{M_{max}} \end{aligned} \tag{18}$$

where, K_b is a nondimensional function that depends on cyclic load magnitude (ζ_b), K_c is a nondimensional function that depends on cyclic load type (ζ_b). Figure 4 shows curves obtained based on the tests results for K_b and K_c. Leblanc et al. [7] defined the cyclic load characteristics as follows and as shown in Figure 5

where M_{max} is the maximum applied moment in a load cycle, and M_{min} is the minimum applied moment in a load cycle, and M_R is the static moment capacity, which was defined by $\hat{\theta} = 4°$ in the nondimensional monotonic moment-rotation curve. The parameter ζ_b measure the amplitude of the cyclic load with respect to static moment capacity. Its value follows $0 < \zeta_b < 1$. The parameter ζ_C describes cyclic load type and its value $\in [1, -1]$ and takes a value of 1 for monotonic loading, a value of 0 for one-way cyclic loading, a value of -1 for symmetric two-way cyclic loading, and a value between 0 and -1 for asymmetric two-way cyclic loading.

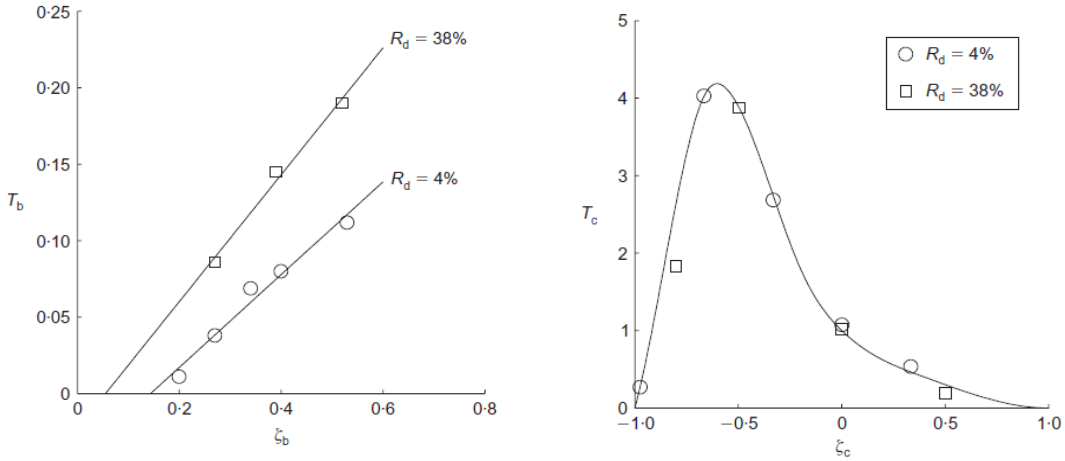

Figure 3. Non-dimensional parameters Tb and Tc according to Leblanc et al. [7]

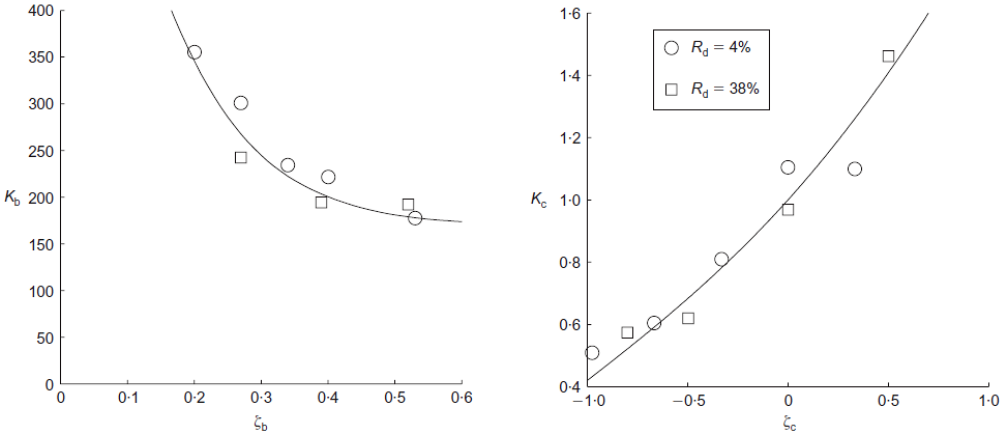

Figure 4. Non-dimensional functions Kb and Kc according to Leblanc et al. [7]

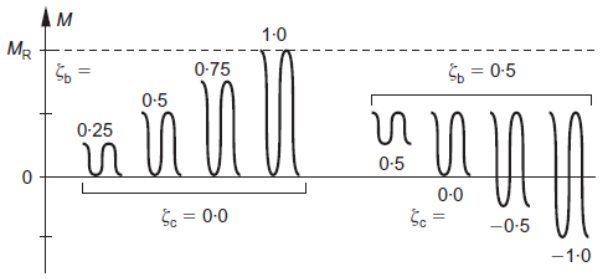

Figure 5. Cyclic load characteristics according to LeBlanc et al. [7]

Based on the results of 1g experimental investigations conducted by Peralta et al., it was demonstrated that the power law originally developed by Little & Briaud [15] in Equation 4 is effective in predicting the accumulated cyclic displacement of laterally loaded rigid piles, with a cyclic degradation parameter value of 0.12 [19-22]. This finding was corroborated by several authors, including Klinkvort et al. [23], Nicolai, & Ibsen [24], and Li et al. [25], through centrifuge and field tests. The field test results from Li et al. [21] indicated a slightly larger cyclic degradation parameter value of 0.085, compared to that found by Little & Briaud [15]. Additionally, centrifuge test results from Klinkvort et al. [23] and Li et al. [25] showed that the cyclic degradation parameter is influenced by the cyclic load magnitude ratio (ζ_b) and cyclic load type ratio (ζ_c), leading to the introduction of Equation 20 to represent this parameter. However, the results of centrifuge tests also indicated that the cyclic degradation parameter depends solely on soil density and the cyclic load type ratio (ζ_c), suggesting that it is not affected by the cyclic load magnitude ratio (ζ_b). Thus, Equation 20 was proposed to describe the cyclic degradation parameter with this updated dependency.

$$\alpha(\zeta_b, \zeta_c) = T_c(\zeta_c).T_b(\zeta_b) \tag{19}$$

$$\alpha_y = (0.3 - 0.22D_r)[1.2(1 - \zeta_c^2)(1 - 0.3\zeta_c)] \quad D_r > 0.5 \tag{20}$$

Previous studies (e.g., Nicolai et al. [24], Li et al. [25], Frick et al. [26], Albiker et al. [27], Truong et al. [28] Li et al. [29]) performed 1g experimental tests on piles embedded in sand, and their findings confirmed that the power formula proposed by Leblanc et al. [7] aligns well with experimental results. These studies also reinforced Leblanc's observation that the most damaging cyclic loading is asymmetric two-way cyclic loading. According to particle image velocimetry (PIV) observations by Frick et al. [26], the increased accumulation rate under asymmetric two-way cyclic loading is attributed to minimal net soil densification around the pile. Richards et al. [30] found that the cyclic accumulation parameter is primarily dependent on soil density and the cyclic load type ratio (ζ_c) and is not sensitive to the cyclic load magnitude ratio (ζ_b). Furthermore, the maximum values of the nondimensional parameter Tc were lower than those reported by Leblanc et al. [7], with the highest values occurring for very loose sand. It was also noted that the strain type variable influences the critical response to asymmetric two-way cyclic loading. These findings emphasize the importance of soil density and load type in influencing cyclic displacement and underline the specific impact of asymmetric loading on pile behaviour.

Arshad et al. [26] conducted a series of 1-g experimental tests on a monopile embedded in dense sand, revealing significant findings regarding the effects of cyclic loading on accumulated displacement. The results demonstrated that, at a constant cyclic amplitude (ζ_b = 0.42), asymmetric two-way cyclic loading (ζ_c = -0.5) induced an accumulated displacement 1.55 times greater than that caused by one-way cyclic loading. Furthermore, at a lower constant amplitude (ζ_b = 0.28), asymmetric two-way cyclic loading resulted in an accumulated displacement 4.5 times larger than that from one-way cyclic loading. The tests also showed that the cyclic secant stiffness of the pile-soil system consistently increased with the number of loading cycles due to soil densification around the pile. However, the secant stiffness decreased as the number of loading cycles increased due to the continuous accumulation of rotation. The proposed logarithmic formula was found to fit the experimental data more accurately than the power law. Additionally, it was observed that the lateral soil resistance distribution, derived from bending strain data, could be misleading. Equations 21 present both the logarithmic and power formulas developed from the experimental results.

$$\frac{\Delta\theta_N}{\theta_0} = \alpha_1 \ln N + \beta_1 \tag{21}$$

where α_1 and β_1 are nondimensional model parameters that are generalized as a function of cyclic load amplitude (ζ_b) and cyclic load type (ζ_c), respectively.

Contrary to current guidelines that suggest a degradation of the secant stiffness of the pile-soil system due to cyclic loading, several studies (e.g., Klinkvort et al. [23] and Nicolai et al. [24]) have supported Leblanc's finding that the cyclic secant stiffness of the pile-soil system actually increases logarithmically with the number of cycles, as proposed in equation 17. Li et al. [25] observed that the cyclic secant stiffness increases exponentially with the number of cycles, as described in Equation 22. Furthermore, they noted that the rate of increase in secant stiffness accelerates when the load type transitions from one-way to two-way cyclic loading. Additionally, increasing the cyclic load amplitude (ζ_c) was found to enhance the accumulation rate of the secant stiffness, further emphasizing the significant impact of loading conditions on the pile-soil interaction. These findings suggest that the pile-soil system exhibits a more complex response to cyclic loading than traditionally assumed, with the secant stiffness showing a tendency to increase under certain cyclic conditions.

$$\frac{K_N}{K_1} = N^{\beta} \tag{22}$$

where K_1 is the initial cyclic secant stiffness, and β is the accumulation rate of cyclic secant stiffness, dependent on cyclic load magnitude ratio ζb and cyclic load type ratio (ζc) as described in Equation 23.

$$\beta(\zeta_b, \zeta_c) = R_c(\zeta_c).R_b(\zeta_b) \quad (23)$$

$$R_b(\zeta_b) = 0.023 - 0.111\zeta_b + 0.266\zeta_b^2 \quad (24)$$

$$R_c(\zeta_c) = 1.31 - 1.1\zeta_c \quad (25)$$

$$K_1 = K_c(\zeta_c).K_s(\zeta_b) \quad (26)$$

$$K_s = (72 - 56\zeta_b) \times 100 \quad \text{kN/m} \quad \text{from monotonic test} \quad (27)$$

$$K_c(\zeta_c) = 0.057\zeta_c + 1.25 \quad \text{from cyclic tests} \quad (28)$$

where K_s and K_c are not relative density-dependent.

A large-scale 1g model test was conducted on an open-ended monopile subjected to unidirectional, one-way lateral loading with 2000 load cycles in saturated, very dense sand. The results showed that pile head displacement and rotation progressively increased with the number of loading cycles. Moreover, the lateral secant stiffness decreased as the number of cycles increased, indicating stiffness degradation. These findings demonstrate that pile head displacement, rotation, and lateral stiffness are significantly influenced by the cyclic loading history, underscoring the importance of accounting for load cycles in the analysis of monopile behaviour under lateral loading [19].

The bearing and deformation behaviour of piles under both monotonic and cyclic loading have been investigated through 1g model tests and numerical simulations. This study examined the effects of loading height, soil relative density, and displacement amplitude on the lateral performance of piles, as well as deformation of the surrounding soil. The monotonic load-displacement and bending moment curves showed similar patterns across varying loading heights and soil densities. Specifically, increasing the loading height from 1D to 4D reduced the horizontal bearing capacity by approximately 1.63 to 1.9 times, while peak bending moment increased by 22.9% to 36.8%. The influence of loading height diminished with increasing soil relative density. Under cyclic loading, the peak load at the pile top increased by 31.7% to 56.1% for each 1 mm increase in displacement amplitude. Soil stiffness around the pile initially decreased then gradually increased with load cycles; after 10,000 cycles, stiffness rose by 23.1% at 50% relative density but did not fully recover at 70% and 90%. Pile displacement increased with both horizontal load and number of cycles but decreased as soil relative density increased. Displacement approached nearly zero at a depth of 14.6D, typical of flexible piles. With greater load and cycles, the soil displacement zone extended downward, eventually covering the entire lower portion of the pile model. These findings emphasize the significant impact of loading conditions and soil properties on pile behaviour under lateral loads [20].

A comprehensive series of 1-g cyclic tests on monopiles embedded in medium-dense sand has provided deep insight into their response under lateral cyclic loading, examining accumulated displacement, cyclic stiffness, bending moments, and reloading behaviour. From the cyclic load-displacement curves measured at the mudline, a theoretical framework was developed to describe the monopile's hysteresis characteristics, leading to the proposal of a novel model for predicting accumulated displacement. Results indicate that accumulated displacement grows with the number of load cycles following a power law, with the rate influenced by key loading parameters but largely unaffected by certain soil stiffness ratios. The normalized cyclic secant stiffness evolves logarithmically, increasing with some loading factors while decreasing with others. The maximum bending moment is primarily governed by the ratio of loading period to pile length, increasing substantially when this ratio nears two, but decreasing when it is below one. Reloading curves typically reconnect with the initial backbone curve beyond the maximum historic cyclic load, with the elastic segment lengthening as specific stiffness parameters increase, though some reloading effects remain not fully understood. Validated against experimental data, the proposed analytical model, which incorporates loading conditions and pile-soil stiffness interactions, enhances the prediction accuracy of accumulated displacement and provides improved guidance for the preliminary design of offshore monopile foundations in sandy soils [21].

Table 1 concludes some of the empirical models proposed based on 1g, centrifuge, and field tests of cyclic laterally loaded piles by after-mentioned researchers:

Table 1. Empirical models based on 1g and centrifuge investigations

Authors	Test type	Number of cycles	Model	Parameters	Critical cyclic load	$T_{c,\,max}$
Leblanc et al. [7]	1g	7400 -65370	$\frac{\Delta\theta}{\theta_S} = T_b(\zeta_b, D_r).\ T_c(\zeta_c).N^{\alpha}$	$T_b(\zeta_b, Dr = 0.04) = 0.414\zeta_b - 0.023$ $T_b(\zeta_b, Dr = 0.38) = 0.414\zeta_b - 0.023$ $T_c(\zeta_c) = * a\zeta_c^4 + * b\zeta_c^3 + * c\zeta_c^2 + * d\zeta_c + * e$ $\alpha = 0.31$	Asymmetric two-way (ζ_c=-0.6)	4
Peralta et al. [22]	1g	5000-10000	* For rigid piles: $y_N = y_1.N^m$ * For flexible piles: $y_N = y_1.(1 + t \ln N)$	m =0.12, t = 0.21	-	-
Klinkvort et al. [23]	25g-75g	250-10000	$\tilde{y}_{max,N} = \tilde{y}_{max,1} \times N^{\alpha}$	$\alpha(\zeta_b, \zeta_c) = T_c(\zeta_c).T_b(\zeta_b)$ $T_b(\zeta_b) = 0.61\zeta_b - 0.013$ $T_c(\zeta_c) = (\zeta_c + 0.63)(\zeta_c - 1)(\zeta_c - 1.64)$	0ne-way	1
Nicolai et al. [24]	1g	50000	$\frac{\Delta\theta}{\theta_0} = T_b.\ T_c.N^{\alpha}$	$\alpha = 0.13$ T_b ,& T_c from curves	Asymmetric two-way (ζ_c=-0.5)	1.4
Li et al. [25]	field	5017- 3173	$y_N = y_1.N^{\alpha}$ $y_N = y_1.(1 + b\ ln(N))$	a= 0.085, b= 0.125	-	-
Arshad et al. [26]	1g	6000	$\frac{\Delta\theta_N}{\theta_0} = \alpha_1\ ln\ N + \beta_1$	$\alpha_1(\zeta_c), \beta_1(\zeta_b)$ from curves $\alpha_{1,max}$ = 2.5	Asymmetric two-way (ζ_c=-0.5)	-
Albiker et al. [27]	1g	2500	$\frac{\Delta\theta}{\theta_S} = T_b(\zeta_b, D_r).\ T_c.N^{\alpha}$ $\frac{\Delta y}{y_S} = T_b(\zeta_b, D_r).\ T_c.N^{\alpha}$	α = 0.23 for rotation & displacement	Asymmetric two-way (ζ_c=-0.5) for rotation (ζ_c=-0.33) for displacement	2.5 1.86

* Polynomial coefficients of: T_c ($\zeta_c \leq$ -0.3): a= 113.33; b= 288.5; c= 238.88; d= 73.48; & Tc ($\zeta_c >$ -0.3): a= 3.06; b= -6.5; c= 5.22; d= -2.76 ; e= 0.99 .

Table 1. Empirical models based on 1g and centrifuge investigations

Authors	Test type	Number of cycles	Model	Parameters	Critical cyclic load	$T_{c,max}$
Truong et al. [28]	60g 250g	50-1500	$y_N = y_1.N^{\alpha_Y}$	$\alpha_y = (0.3 - 0.22D_r)[1.2(1-\zeta_c^2)(1-0.3\zeta_c)]$	Asymmetric two-way (ζ_c=-0.5)	-
Li et al. [29]	100g	42-152	$\frac{y_{max,N}}{Y_{max,a}} = N^{\alpha}$	$\alpha(\zeta_b,\zeta_c) = T_c(\zeta_c).T_b(\zeta_b)$ $T(\zeta_b) = 0.07335$ $T_c(\zeta_c) = -1.707(\zeta_c + 0.31)^2 + 0.949$ $(D_r = 80\%)$ $T_c(\zeta_c) = -1.14(\zeta_c + 0.323)^2 + 1.263$ $(D_r = 50\%)$	Asymmetric two-way (ζ_c=-0.4)	1.25
Richards et al. [30]	1g	1000-10000	$\epsilon = A.N^{\alpha}$ * Rotation: $\frac{\Delta\theta_{M\ or\ P}}{\theta_S} = T_b(\zeta_b, D_r).T_c(\zeta_c).N^{\alpha}$ * Displacement: $y_N = y_1.N^{\alpha_Y}$	for $\theta_{m,\alpha}$ = 0.26 for θ_P, α = 0.3 α_y is the same as Troung et al. (2018).	Asymmetric two-way (ζ_c=-0.6) for rotation (ζ_c=-0.5 for displacement	2.9
Fick et al. [31]	1g	2500-10000	$y_N = y_1.N^{\alpha(\zeta_c)}$	$\alpha(\zeta_c) = 0.0958 - 0.0858\zeta_c - 0.1576\zeta_c^2 + 0.1476\zeta_c^3$,** LB $\alpha(\zeta_c) = 0.14 - 0.1466\zeta_c - 0.1176\zeta_c^2 + 0.1238\zeta_c^3$,** UB	Asymmetric two-way (-0.15<ζ_c<-0.4)	-

** LB means the lower boundary of accumulation coefficient $\alpha(\zeta_c)$; ** UB means the upper boundary of accumulation coefficient $\alpha(\zeta_c)$.

Due to significant discrepancies in the literature regarding changes in pile-soil stiffness caused by cyclic loading and the most damaging cyclic load type (one-way or asymmetric two-way), this paper presents 1-g experimental tests on a small-scale monopile model to provide deeper insight into the changes in accumulated pile rotation and pile-soil stiffness resulting from cyclic loading.

2. 1-G Experimental Small-Scale Tests

Figure 6 illustrates the flowchart of the research methodology.

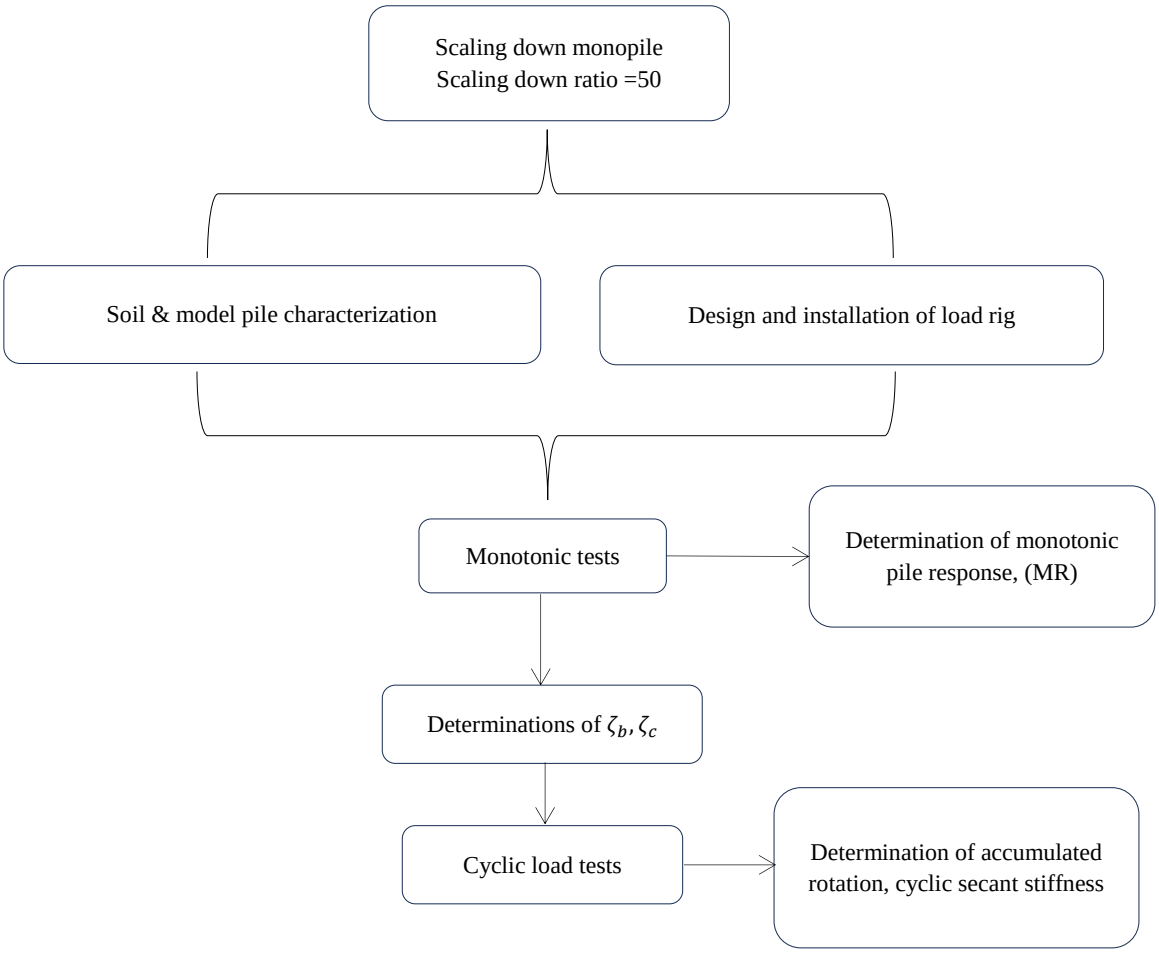

Figure 2. Methodology flow chart

2.1. Load Rig

The load rig is the same as that installed initially by Rovere et al. [32] and used by Leblanc et al. [7]. The load rig is stable and can generate millions of load cycles. As shown in Figure 7, the load rig consists of the following:

- Steel frame and rectangular tank with dimensions (90×90×80 cm).
- Bin loading arm oscillates vertically [6].
- pulleys and high tensile wires [4, 5].
- AC gear motor rotates 6 Rev/min (frequency = 0.1 cycle/s) [1].
- Two LVDTs with an accuracy of 0.005 mm [3].
- Load cell LP7141-200KG-C3 [2].
- Instru-Net data acquisition system.
- Loading hanger and weights [7, 8].

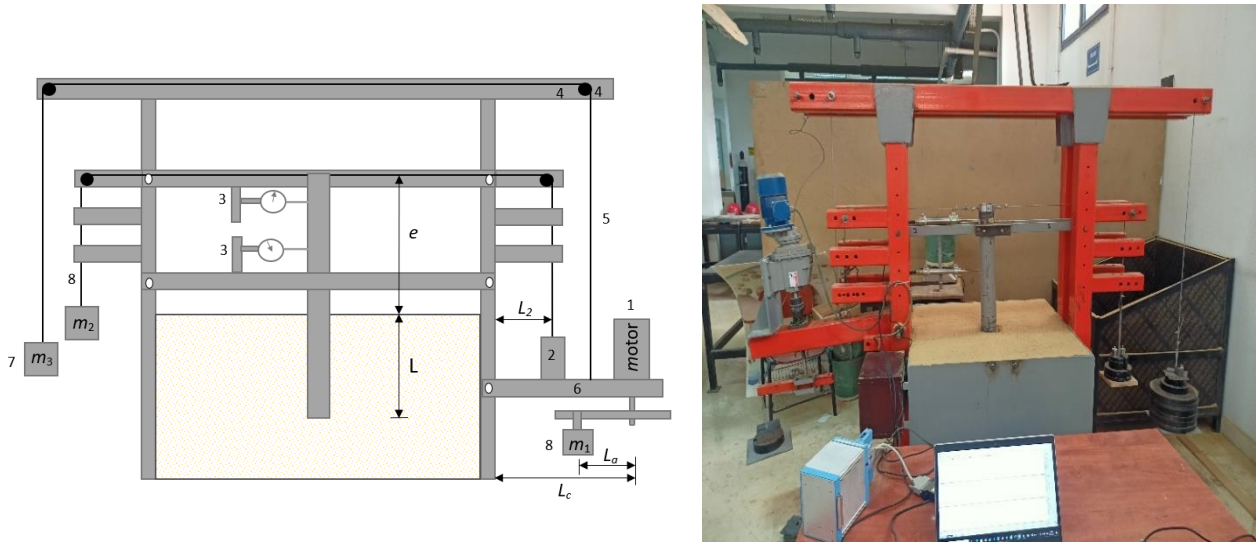

Figure 3. Cyclic Load Rig

The weight m3 is used to counterbalance the weight of the loading beam and AC gear motor, which is 67.5 kg. The weights m1 and m2 are used to generate a sinusoidal cyclic load on the model pile according to Equation 29. When the weight m1 rotates, the center of mass of the pin loading beam changes, so it oscillates sinusoidally in the vertical direction. To apply a sinusoidal load to the pile, m1 and m2 are selected appropriately as presented in Equations 30 and 31.

$$H(t) = H_O + H_a \sin(\omega t) \tag{29}$$

$$\mathrm{m_1} = \left(\frac{\mathrm{l_2}}{\mathrm{l_a}}.\mathrm{H_a}\right).\frac{1}{\mathrm{g}} \tag{30}$$

$$\mathrm{m_2} = \left(\frac{\mathrm{l_c}}{\mathrm{l_a}}.\mathrm{H_a} - \mathrm{H_o}\right).\frac{1}{\mathrm{g}} \tag{31}$$

2.2. Soil Properties and Preparation

The used soil is loose and medium-dense silica sand. A dry sieve analysis test is performed in the laboratory to determine the grain size distribution curve. A Proctor test is performed to determine the maximum dry density, while the minimum dry density is determined from a standard calibration jar by pouring the sand from a very low height. Four direct shear tests were performed to determine the peak angle of internal friction for each soil state (loose and medium dense). At each test, the sand samples are subjected to the following normal stresses: 0.0278, 0.0556, 0.0833, and 0.111 kg/cm^2. Table 2 shows the soil properties investigated.

Table 2. Soil properties

Property	Value
Particle size d_{10}, d_{30}, d_{50}, d_{60} mm	0.2, 0.35, 0.5, 0.6
Specific Gravity G_s"	2.65
Minimum dry unit weight γ_{min} (kN/m^3)	15
Maximum dry unit weight γ_{max} (kN/m^3)	17.5
Peak angle of internal friction for loose sand (Dr =8%), $Ø_{peak}$, degrees	30
Peak angle of internal friction for medium sand (Dr =34%), $Ø_{peak}$, degrees	34

The required sand mass to fill the tank to reach the required density was weighed and put on three layers in the tank and compacted by tamping to reach the required density. The loose sand (D_r = 8%) was poured from a low height.

2.3. Model Pile

The mode pile used in the tests is an open-end steel tube, and according to Polous and Hull [12], this model pile is classified as a rigid pile. The pile properties are illustrated in Table 3.

Table 3. Model pile properties

Property	Value
Pile diameter (d) mm	90
Wall thickness (t) mm	2
Penetration length (L) mm	450
Load eccentricity (h) mm	535, 385, 235
Pile Weight (W) N	47
Flexural stiffness (EI) KN. m^2	58.14

Initially, the pile was aligned vertically in the center of the tank using two sides supports, as shown in Figure 8-b. Then, the pile was driven in the soil mass using a hammer with a rubber head falling from a constant height, as shown in Figure 8-a. The number of blows required to reach the required penetration depth in the medium dense state is 500 ± 25, while the number of blows required to reach the required penetration depth in the loose state is 250 ±25.

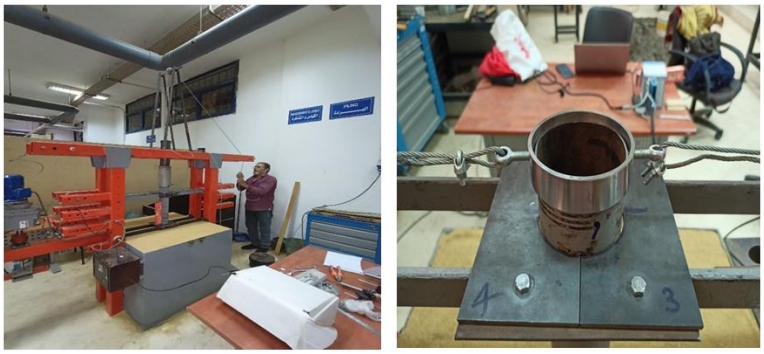

(a) (b)

Figure 8. Pile installation: (a) pile driving; (b) side supports

2.4. Monotonic Tests

The monotonic loading was performed incrementally without operating the AC motor. The mass m_1 was increased incrementally by 0.5 kg every 5 mins, but the mass m_2 was zero, and according to Abadie et al. [33], the creep effects can be neglected during this time.

2.5. Cyclic Tests

The cyclic test was performed by operating the AC motor. When m_1 rotates, the main load beam oscillates vertically and generates a later cyclic load on the pile head. The masses m_1 and m_2 are chosen according to the planned cyclic load characteristics (ζ_b & ζ_c). Figure 5 shows the cyclic load test of the pile.

2.6. Tests Program

Table 4 illustrates the tests program performed in the Future University geotechnical laboratory.

Table 4. Laboratory test program

System	Type	L (mm)	h (mm)	D_r (%)	ζ_b	ζ_c	N
1	Monotonic	450	535	8	-	-	-
	Monotonic		385	8	-	-	-
	Monotonic		235	8	-	-	-
	Cyclic		535	8	0.26	0	10000
	Cyclic		535	8	0.34	0	10000
	Cyclic		535	8	0.53	0	10000
	Cyclic		535	8	0.6	0	10000
	Cyclic		535	8	0.417	-0.23	10000
	Cyclic		535	8	0.417	-0.5	10000
	Cyclic		535	8	0.417	-0.6	10000
	Cyclic		535	8	0.417	-0.7	10000
	Cyclic		535	8	0.417	-0.98	10000

	Monotonic		535	34	-	-	-
	Monotonic		385	34	-	-	-
	Monotonic		235	34	-	-	-
	Cyclic		535	34	0.248	0	10000
	Cyclic		535	34	0.417	0	10000
2	Cyclic	450	535	34	0.58	0	10000
	Cyclic		535	34	0.77	0	10000
	Cyclic		535	34	0.417	-0.25	10000
	Cyclic		535	34	0.417	-0.575	10000
	Cyclic		535	34	0.417	-0.82	10000
	Cyclic		535	34	0.417	-0.95	10000

2.7. Scaling Up Considerations

It is well known that the governing Behavior of sand is frictional, and this behavior is mainly governed by the isotropic stress level [34]. In addition, the soil stiffness is stress-dependent. Due to all the tests being performed in the 1g lab, the isotropic stress is much lower than in the field. Therefore, the scaling-up method considered by Leblanc et al. [7] is used here. This method is as follows:

- The sand sample in the lab is prepared at a lower relative density to ensure that the peak angle of internal friction in the lab is similar to that of the field.
- The stiffness stress dependency is accounted for by expressing shear modulus as follows:

$$\frac{G}{p_a} = C_1 . \left(\frac{\acute{\sigma}_v}{p_a}\right)^n \quad (32)$$

where p_a is the atmospheric pressure, C_1 is the nondimensional constant, n is the pressure coefficient with a recommended value equal to 0.5, and $\acute{\sigma}_v$ is the effective vertical stress at depth C_2L below the seabed.

$$\acute{\sigma}_v = C_2 . L . \acute{\gamma}$$

- Grain size effects on soil-structure interaction will be nonsignificant if the ratio between the pile diameter and the mean diameter of sand particle (D/d_{50}) > 60 [35]. In this paper, the (D/d_{50}) = 180; therefore, the grain size effect is negligible.

The scaling-up ratio of the tested model piles is 50, which means that this model corresponds to a prototype of diameter 4.5 m and 22.5 m embed length for scaling geometric and dynamic similarity, while kinematic similarity can be neglected due to low cyclic loading frequency. The nondimensional products developed by Leblanc et al. [7], as shown in Table 5, are adopted here.

Table 5. Nondimensional products adopted by LeBlanc et al. [7]

Nondimensional Parameters	
Moment Loading	$\tilde{M} = \frac{M}{L^3 . d . \acute{\gamma}}$
Vertical Force	$\tilde{V} = \frac{V}{L^2 . d . \acute{\gamma}}$
Horizontal Force	$\tilde{H} = \frac{H}{L^2 . d . \acute{\gamma}}$
Rotation (degrees)	$\tilde{\theta} = \theta . \sqrt{\frac{p_a}{L . \acute{\gamma}}}$
Load eccentricity	$\tilde{h} = \frac{M}{HL}$
Aspect ratio	$\eta = \frac{L}{d}$

3. Results and Discussion

3.1. Monotonic Response

As shown in Figure 9, for the two sand relative densities (Dr = 8% and Dr = 34%), the monopile rotation and moment both increase continuously without reaching a plateau and it was found that the pile deformation response becomes

stiffer with increasing sand relative density. The monotonic moment rotation response of the model pile is fitted well by the power formula as described in Equations 33 and 34 for loose and medium-dense sand, respectively

$$M = 77.37\ \theta^{0.408} \quad (33)$$

$$M = 44.6\ \theta^{0.367} \quad (34)$$

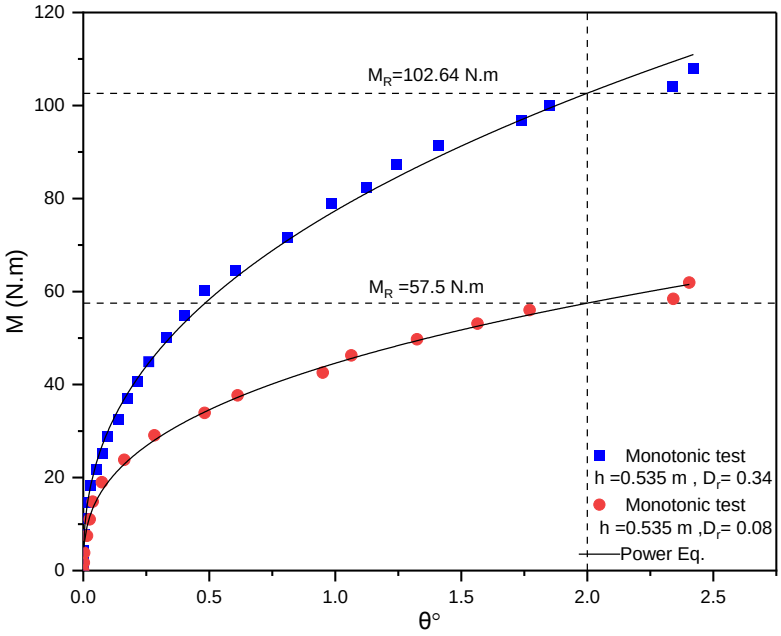

Figure 9. Monotonic moment-rotation curve

3.2. Failure Criteria

It is so difficult to determine the point of failure of the model pile. Several failure criteria were adopted in previous research, such as the change of slope criterion, which captures the point of failure at the point at which the slope of the load-displacement curve starts to change [22]; deformation criteria, which define the failure point at certain displacement or rotation [4] and lastly hyperbolic formula criterion which define the moment -rotation or load-displacement curve into hyperbola and the point of failure can be capture by extrapolating [36]. Table 6 shows the failure criteria adopted by previous authors. In this paper, the deformation criterion was adopted, which assumes that the pile fails after reaching a 2° rotation. This criterion has been widely accepted by researchers such as Lee et al. [37], PISA [17], and Richards et al. [30].

Table 6. Failure criteria adopted by previous researchers

Reference	Failure criteria
Peralta et al. [22]	$y_{mud} = 0.1$ L
Leblanc et al. [7]	$\tilde{\theta} = \theta_{ref.}\sqrt{\frac{p_a}{\dot{\gamma}}} = 4°$
Klinkvort et al. [23]	$\theta = 4°$
Truong et al. [28]	$\theta = 0.5°$
Arshad et al. [26]	$\theta = 1.5°$
Al biker et al. [27]	$\theta = 3°$
Frick et al. [38]	Hyperbolic formula (Manolui et al. [36])
Li et al. [29]	$y_{mud} = 0.075D$
Lee et al. [37], PISA [17], Richards et al. [30]	$\theta = 2°$

The lateral moment resistance (M_R) of the model pile increases with increasing sand relative density, as shown in Figure 8. Specifically, the M_R was found to be 102.64 N·m in medium-dense sand (Dr = 34%) and 57.5 N·m in loose sand (Dr = 8%).

3.3. Cyclic Response

3.3.1. Accumulated Rotation

As seen in Figures 10 and 11, the pile lateral accumulated displacement increases with a number of load cycles in medium dense and loose sand states, and the power formula proposed by Leblanc et al. [7] and introduced in equation (16) fits the results well but with different nondimensional parameters (α, T_b and T_c) values. It was observed that most of the drawings of accumulated rotation versus number of cycles are parallel so that the accumulation parameter (α) can be considered constant with an overall average value equal to 0.09, which is lower than the value observed by LeBlanc et al. [7] and may be the reason for this discrepancy that the accumulation parameter α is material dependent but is still in the range between 0.074 and 0.31 which is provided in the literature.

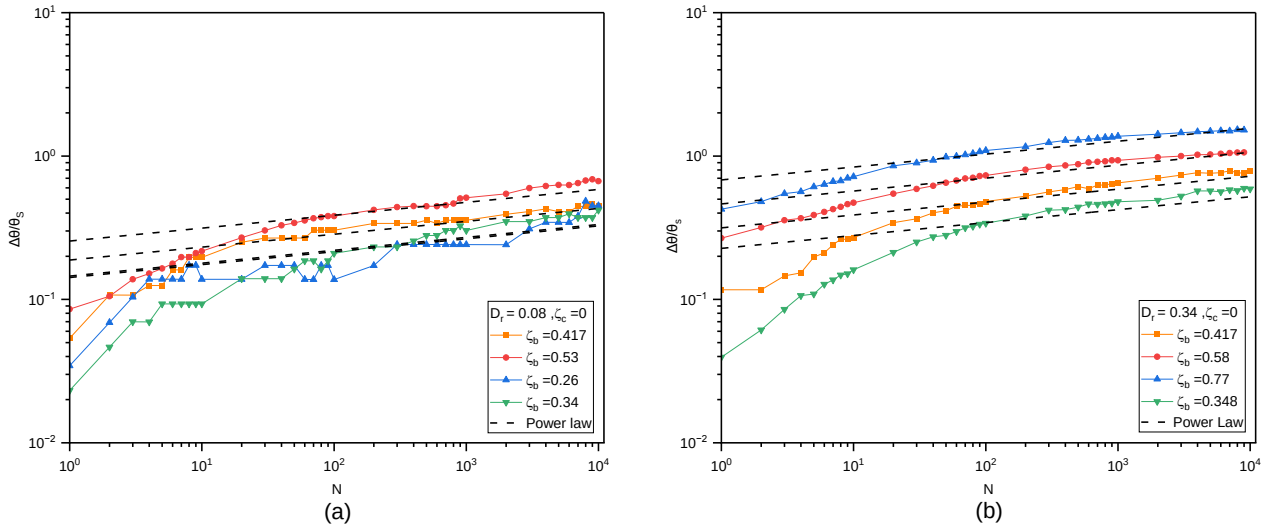

Figure 10. Accumulated displacement due to one-way cyclic load (ζ_c =0): (a) D_r=8%;(b) D_r=34%

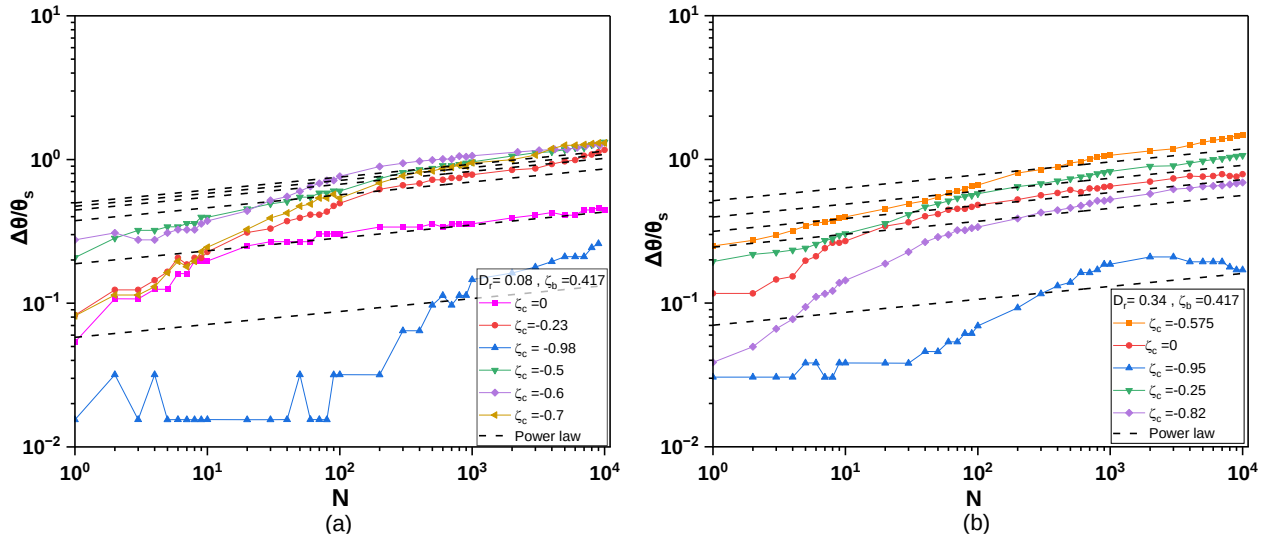

Figure 11. Accumulated displacement due to two-way cyclic load (ζ_b =0.417): (a) D_r=8%;(b) D_r=34%

Notably, the pile accumulated rotation increases with increasing the cyclic load magnitude ratio (ζ_b), as shown in Figure 10. The effect of cyclic load magnitude load ratio was considered in the power formula by using the nondimensional parameter (T_b). This parameter (T_b) is dependent on cyclic load magnitude ratio (ζ_b); it linearly increases with increasing cyclic load magnitude ratio (ζ_b) with larger values in medium dense sand than loose sand as seen in Figure 12 and Equations 35 and 19 provide correlations for this parameter in loose and medium dense sand respectively.

$$T_b = 0.022 + 0.47\zeta_b \qquad D_r = 0.08 \tag{35}$$

$$T_b = 0.058 + 0.78\zeta_b \qquad D_r = 0.34 \tag{36}$$

$$T_c = 1.013 - 6.47\zeta_c - 4.04\zeta_c^2 + 3.165\zeta_c^3 \qquad D_r = 0.08 \tag{37}$$

$$T_c = 0.98 - 1.06\zeta_c + 3.3\zeta_c^2 + 5.58\zeta_c^3 \qquad D_r = 0.34 \tag{38}$$

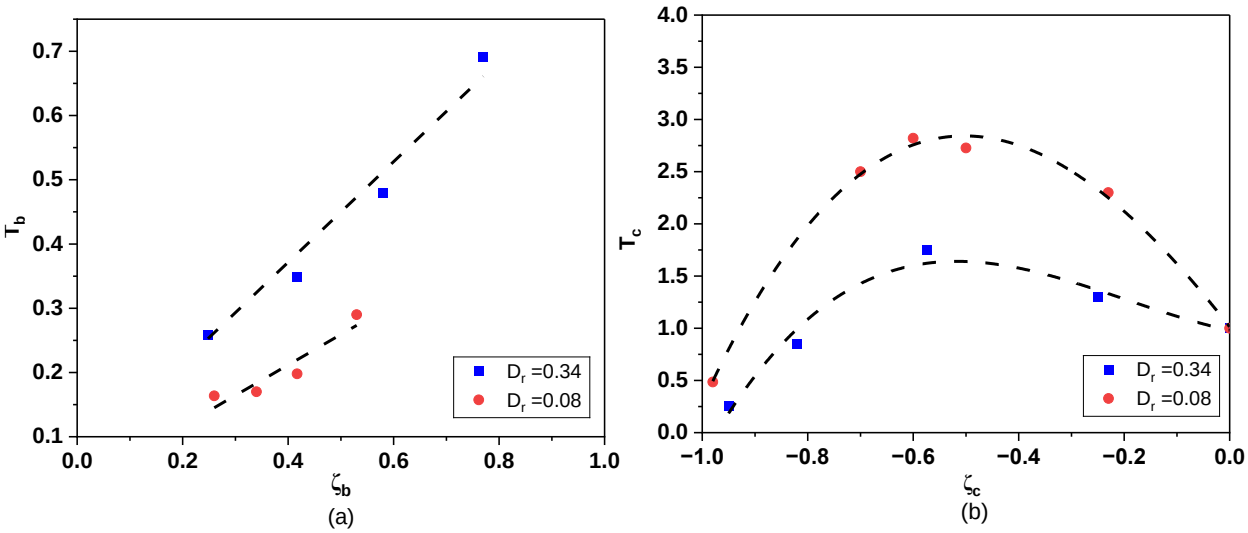

Figure 12. Nondimensional constants: (a) T_b ; (b) T_c

For a constant cyclic load magnitude ratio (ζ_b) of 0.417, corresponding to the extreme loading conditions of offshore wind turbines [39], the maximum accumulated displacement occurs under asymmetric two-way cyclic loading with a cyclic load type ratio (ζ_c) of –0.6, as shown in Figure 12. This observation aligns with the findings of previous studies (e.g., Leblanc et al. [7]; Nicolai et al. [24]; Albiker et al. [27]; Truong et al. [28]; Li et al. [29]; Frick et al. [38]) and may be attributed to minimal soil compaction around the pile under this loading condition. Figure 12 illustrates that the nondimensional constant T_c depends on the cyclic load type. Specifically, T_c increases as the cyclic load type ratio (ζ_c) changes from 0 to –0.6, reaching peak values of 2.7 and 1.7 for loose and medium-dense sand, respectively, before decreasing again. This peak corresponds to the asymmetric two-way cyclic load. Furthermore, the maximum value of (T_c) is higher for loose sand compared to medium-dense sand, indicating that T_c is also dependent on soil relative density. Based on curve fitting, a cubic polynomial describes the relationship between T_c and ζ_c, as provided in Equations 37 and 38 for medium-dense and loose sand, respectively.

As shown in Figures 13 and 14, the cyclic secant stiffness of the pile-soil foundation system increases with the number of load cycles, likely due to soil densification around the pile caused by cyclic loading. The logarithmic formula developed by LeBlanc et al. [7], as provided in Equation 17, is used to fit the results. However, the overall average value of the nondimensional coefficient A_k equals 7.2, slightly lower than the value reported by LeBlanc et al. [7].

This formulation fits the data only partially due to the large scatter in results, which may stem from the measurement of very small changes in pile displacement between successive cycles. Such minimal variations can introduce inconsistencies or noise, especially when displacement changes fall within the limits of measurement precision, making it challenging to accurately capture the pile's stiffness response during cyclic loading. It was also observed that cyclic secant stiffness decreases with increasing cyclic load magnitude ratio (ζ_b) and as the cyclic load type changes from one-way to two-way cyclic loading. This behaviour may be due to the initial cyclic secant stiffness (K_0) decreasing with increasing (ζ_b) for one-way cyclic loading (ζ_c=0), as shown in Figure 13, and further decreasing when transitioning from one-way to two-way cyclic loading at a constant cyclic magnitude ratio (ζ_b=0.417), as shown in Figure 14. According to equation (20), the initial cyclic stiffness depends on non-dimensional functions K_b and K_c, which are mainly influenced by cyclic load magnitude ratio (ζ_b) and cyclic load type ratio (ζ_c), respectively, as presented in Equations 39 and 40 and illustrated in Figure 15.

$$K_b = 157\zeta_c^2 - 263\zeta_c + 202.73 \tag{39}$$

$$K_c = 0.52\zeta_c^2 + 0.97\zeta_c + 0.97 \tag{40}$$

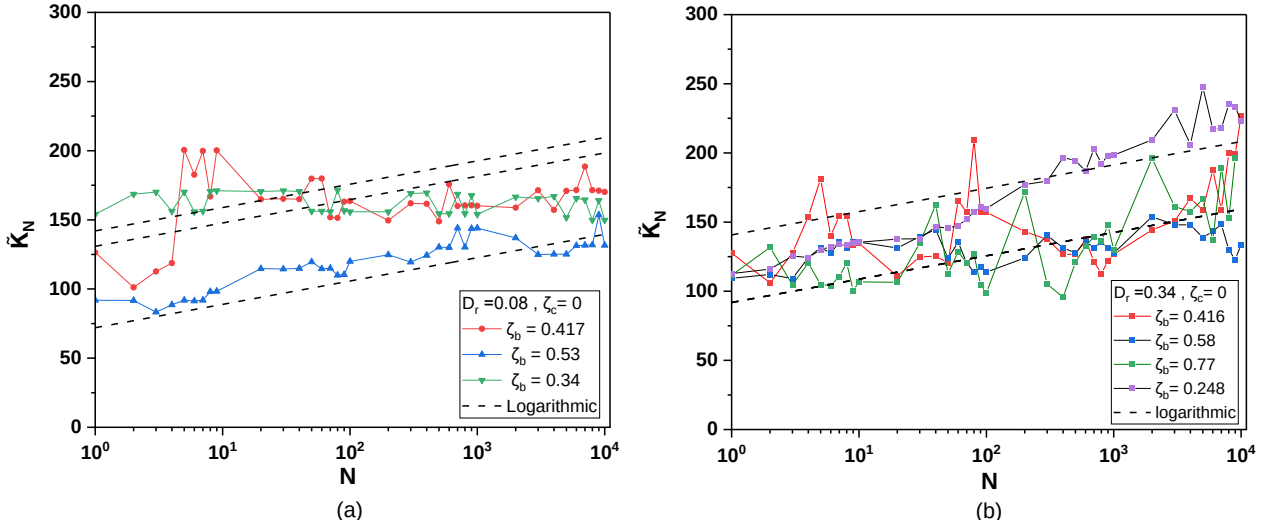

Figure 13. Evolution of cyclic secant stiffness due to one-way cyclic load (ζ_c =0): (a) D_r=8%; (b) D_r=34%

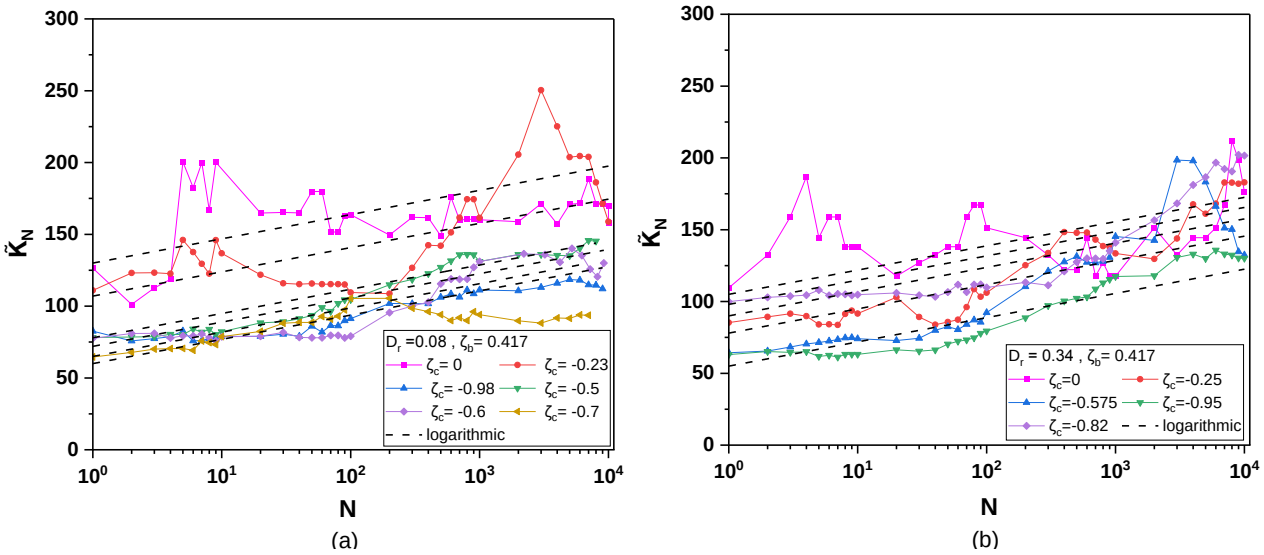

Figure 14. Evolution of cyclic secant stiffness due to two-way cyclic load

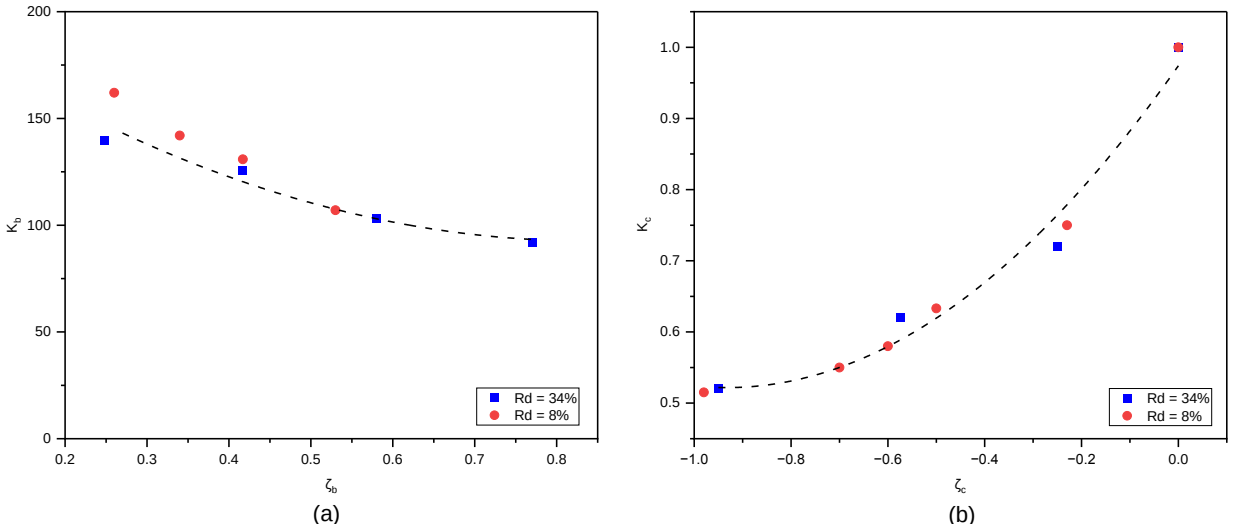

Figure 15. Non-dimensional functions: (a) K_b; (b) K_c

4. Conclusion

This study investigated the lateral cyclic behaviour of monopiles through 1-g experimental tests, focusing on accumulated displacement and cyclic secant stiffness under different loading conditions and soil densities. The results show that the pile's lateral accumulated displacement increases with the number of load cycles, following a power law relationship like that proposed by LeBlanc et al. [7], but with a lower exponent constant (α=0.09). The displacement also increases with higher cyclic load magnitudes, with the nondimensional parameter (T_b) linearly related to the cyclic load magnitude ratio (ζ_b). The maximum displacement occurred under asymmetric two-way cyclic loading (ζ_c=−0.6), consistent with previous findings in the literature, and was strongly influenced by sand relative density, with nondimensional values of 2.7 and 1.7 for loose and medium-dense sand, respectively.

In terms of stiffness, the cyclic secant stiffness of the pile-soil system was found to increase with the number of load cycles but decrease with rising cyclic load magnitude and when transitioning from one-way to two-way cyclic loading. The logarithmic model by LeBlanc et al. [7] provided a reasonable fit to the stiffness data despite significant scatter. These findings emphasize the importance of considering both cyclic load type and soil density when evaluating monopile performance. Further experimental and numerical research is recommended to deepen the understanding of soil-pile interaction effects and to enhance design standards for offshore monopile foundations.

5. Symbols

X_c	Corrected cyclic stress ratio	ζ_b	Cyclic load magnitude ratio
ζ_c	Cyclic load type ratio	σv	The effective vertical
E_pI_p	Pile flexural stiffness	E_s	Soil young's modulus
$p_{(x,y)}$	Soil bedding resistance	p_u	Soil ultimate bedding resistance
X^0	Cyclic stress ratio at initial stress condition	X^1	Cyclic stress ratio after applying first load cycle
y_1	Pile lateral displacement after first cycle	y_N	Pile lateral displacement after N of cycles
$\acute{\gamma}$	Buoyant soil unit weight	θ_S	Static rotation
σ_1^0	Major principal stress at initial stress condition (zero loading condition)	σ_1^1	Major principal stress after applying first load cycle
σ_{1f}^0	Major principal stress at static failure state of initial stress condition	σ_{1f}^1	Major principal stress at static failure state after applying fist load cycle
D_r	Sand relative density	$\tilde{k}$	Nondimensional cyclic secant stiffness
β_2	The accumulation rate of cyclic secant stiffness	$\Delta\theta$	Accumulated rotation
A	Calibration factor	A_k	A nondimensional constant
API	American Petroleum Institute recommended practice for Planning, Designing, and Constructing Fixed Offshore Platforms-Working Stress Design	b_1 and b_2	Material regression parameters
C1, C2, C3	Dimensionless coefficients	D	Pile diameter
DNVGL	Det Norske Veritas and Germanischer Lloyd recommended practice for support structures of offshore wind turbines	E_{s1}	Secant stiffness after first cycle
E_{SN}	Secant stiffness after N of cycles	G	Soil shear modulus
K	Initial stiffness coefficient	K_1	The initial cyclic secant stiffness
K_b, K_C	Dimensionless functions	$K_{h,N}$	Horizontal subgrade reaction modulus after N of cycles
$K_{h,1}$	Determined by static p-y curve	K_h	Horizontal subgrade modulus
$K_{s,N}$	Secant stiffness after N of cycles	$K_{s,1}$	Initial secant stiffness
L	Pile embedded length	M_{max}	The maximum applied moment in a load cycle
M_{min}	The minimum applied moment in a load cycle	M_R	The static moment capacity
n	The pressure coefficient	n_h	Horizontal coefficient of subgrade modulus
p_a	The atmospheric pressure	R_s	Accumulated strain due to cyclic loading
t, a	A cyclic degradation parameter	T	Pile-soil relative stiffness
T_b, T_c,α_1, β_1	Nondimensional parameters	x	Soil depth
y	Pile lateral displacement	α, α_y	An accumulation coefficient
α	A parameter to control relative contribution between soil resistance and deflection	β	Soil density factor
$\varepsilon_{cp,N}$	Axial plastic strain after N of cycles	$\varepsilon_{cp,N=1}$	Axial plastic strain after first cycle
ξ	Pile installation factor	Φ	Cyclic load type factor
$\tilde{k}_0$	Nondimensional initial cyclic secant stiffness		

6. Declarations

6.1. Author Contributions

Conceptualization, R.M.E.; methodology, A.M.E.; validation, S.S.A.; formal analysis, A.M.E.; investigation, S.S.A.; resources, M.M.K.; data curation, S.S.A.; writing—original draft preparation, M.M.K.; writing—review and editing, R.M.E.; experimental work, M.M.K. All authors have read and agreed to the published version of the manuscript.

6.2. Data Availability Statement

The data presented in this study are available on request from the corresponding author.

6.3. Funding

The authors received no financial support for the research, authorship, and/or publication of this article.

6.4. Acknowledgements

I extend my heartfelt thanks to Prof. Dr. Khaled Abd-El Rahman, who generously provided me with valuable theses and research papers that significantly contributed to this study. I am also profoundly grateful to the technical team, particularly Mr. Shaaban and Mr. Sayed, whose dedication and hard work in setting up the load rig and conducting the experimental work were essential to the success of this project. Lastly, I would like to thank Mr. Yaqub El-Mansoori for his assistance in sourcing critical components related to the load rig from the United States, which was instrumental in completing the experimental setup.

6.5. Conflicts of Interest

The authors declare no conflict of interest.

7. References

[1] GWEC. (2023). Global Wind Report 2023. Global Wind Energy Council (GWEC), Lisbon, Portugal.

[2] Li, J., Wang, G., Li, Z., Yang, S., Chong, W. T., & Xiang, X. (2020). A review on development of offshore wind energy conversion system. International Journal of Energy Research, 44(12), 9283–9297. doi:10.1002/er.5751.

[3] Rathod, D., Krishnanunni, K. T., & Nigitha, D. (2020). A Review on Conventional and Innovative Pile System for Offshore Wind Turbines. Geotechnical and Geological Engineering, 38(4), 3385–3402. doi:10.1007/s10706-020-01254-0.

[4] Li, D., Zhao, J., Wu, Y., Zhang, Y., & Liang, H. (2024). An innovative bionic offshore wind foundation: Scaled suction caisson. Renewable and Sustainable Energy Reviews, 191, 114208. doi:10.1016/j.rser.2023.114208.

[5] Wang, Y., Zhu, M., Dai, G., Xu, J., & Wu, J. (2024). Analytical framework for natural frequency shift of monopile-based wind turbines under two-way cyclic loads in sand. Geomechanics and Engineering, 37(2), 167–178. doi:10.12989/gae.2024.37.2.167.

[6] Murchison, J. M., & O'Neill, M. (1983). An evaluation of p-y relationships in sands. Master's thesis, Dept. of Civil Engineering, Cullen College of Engineering. University of Houston-University Park, Dallas, United States.

[7] LeBlanc, C., Houlsby, G. T., & Byrne, B. W. (2010). Response of stiff piles in sand to long-term cyclic lateral loading. Geotechnique, 60(2), 79–90. doi:10.1680/geot.7.00196.

[8] Reese, L. C., Cox, W. R., & Koop, F. D. (1974). Analysis of Laterally Loaded Piles in Sand. Offshore Technology Conference. doi:10.4043/2080-ms.

[9] API RP 2A-WSD 22nd Ed. (2014). Planning, Designing, and Constructing Fixed Offshore Platforms - Working Stress Design. American Petroleum Institute (API), Wahington, United States.

[10] DNVGL-ST-0126. (2018). Support structures for wind turbines. Det Norske Veritas (DNV), Bærum, Norway

[11] Briaud, J. L., Smith, T. O., & Meyer, B. J. (1983). Using the Pressuremeter Curve to Design Laterally Loaded Piles. Offshore Technology Conference. doi:10.4043/4501-ms.

[12] Poulos, H. G., & Hull, T. S. (1989). The role of analytical geomechanics in foundation engineering. Foundation engineering: Current principles and practices. American Society of Civil Engineers (ASCE), Reston, United States.

[13] Abdel-Rahman, K., & Achmus, M. (2005). Finite element modelling of horizontally loaded monopile foundations for offshore wind energy converters in Germany. International Symposium on Frontiers in Offshore Geotechnics (ISFOG), Perth, Australia. doi:10.1201/noe0415390637.ch38.

[14] Davidson, H. L. (1981). Laterally loaded drilled pier research. Electric Power Research Institute (EPRI), Palo Alto, United States.

[15] Gerolymos, N., & Gazetas, G. (2006). Development of Winkler model for static and dynamic response of caisson foundations with soil and interface nonlinearities. Soil Dynamics and Earthquake Engineering, 26(5), 363–376. doi:10.1016/j.soildyn.2005.12.002.

[16] Lam, I. P., & Martin, G. R. (1986). Seismic design for highway bridge foundations. Report No. FHWA/RD-86/102, FHWA, McLean, United States.

[17] Byrne, B., McAdam, R., Burd, H., Houlsby, G., Martin, C., c, L., Taborda, D., Potts, D., Jardine, R., Sideri, M., Schroeder, F., Gavin, K., Doherty, P., Igoe, D., Wood, A., Kallehave, D., & Gretlund, J. (2015). New design methods for large diameter piles under lateral loading for offshore wind applications. Frontiers in Offshore Geotechnics III, 705–710. doi:10.1201/b18442-96.

[18] Little, R. L., & Briaud, J. L. (1988). Full scale cyclic lateral load tests on six single piles in sand. Miscellaneous Paper GL-88-27. Geotechnical Division, Texas A&M University, Texas, United States.

[19] Akdag, C. T., & Rackwitz, F. (2024). Long-term horizontal cyclic loading model test results of monopile for offshore wind turbines. Geotechnical Engineering Challenges to Meet Current and Emerging Needs of Society, 2755–2759. doi:10.1201/9781003431749-536.

[20] Ma, J., Xu, J., Fan, Z., Li, H., & Xu, G. (2024). Bearing and deformation characteristics of monopile foundation under monotonic and cyclic horizontal loads. Science Progress, 107(2), 00368504241260268. doi:10.1177/00368504241260268.

[21] Wang, Y., Dai, G., Li, H., Gao, L., & Li, B. (2025). Lateral response of monopiles under cyclic loading in sand: Laboratory model tests and theoretical studies. Ocean Engineering, 322(October), 120500. doi:10.1016/j.oceaneng.2025.120500.

[22] Peralta, P. (2010). Investigations on the behavior of large diameter piles under long-term lateral cyclic loading in cohesionless soil. PhD Thesis, Leibniz University, Hannover, Germany

[23] Klinkvort, R. T., & Hededal, O. (2013). Lateral response of monopile supporting an offshore wind turbine. Proceedings of the Institution of Civil Engineers - Geotechnical Engineering, 166(2), 147–158. doi:10.1680/geng.12.00033.

[24] Nicolai, G., & Ibsen, L. B. (2014). Small-scale testing of cyclic laterally loaded monopiles in dense saturated sand. International Ocean and Polar Engineering Conference, 15-20 June, 2014, Busan, Korea.

[25] Li, W., Igoe, D., & Gavin, K. (2015). Field tests to investigate the cyclic response of monopiles in sand. Proceedings of the Institution of Civil Engineers: Geotechnical Engineering, 168(5), 407–421. doi:10.1680/jgeen.14.00104.

[26] Arshad, M., & O'Kelly, B. C. (2017). Model Studies on Monopile Behavior under Long-Term Repeated Lateral Loading. International Journal of Geomechanics, 17(1), 1–12. doi:10.1061/(asce)gm.1943-5622.0000679.

[27] Albiker, J., Achmus, M., Frick, D., & Flindt, F. (2017). 1 G Model Tests on the Displacement Accumulation of Large-Diameter Piles Under Cyclic Lateral Loading. Geotechnical Testing Journal, 40(2), 173–184. doi:10.1520/GTJ20160102.

[28] Truong, P., Lehane, B. M., Zania, V., & Klinkvort, R. T. (2019). Empirical approach based on centrifuge testing for cyclic deformations of laterally loaded piles in sand. Geotechnique, 69(2), 133–145. doi:10.1680/jgeot.17.P.203.

[29] Li, Q., Askarinejad, A., & Gavin, K. (2022). Lateral response of rigid monopiles subjected to cyclic loading: centrifuge modelling. Proceedings of the Institution of Civil Engineers: Geotechnical Engineering, 175(4), 426–438. doi:10.1680/jgeen.20.00088.

[30] Richards, I. A., Byrne, B. W., & Houlsby, G. T. (2020). Monopile rotation under complex cyclic lateral loading in sand. Geotechnique, 70(10), 916–930. doi:10.1680/jgeot.18.P.302.

[31] Frick, D., & Achmus, M. (2022). A model test study on the parameters affecting the cyclic lateral response of monopile foundations for offshore wind turbines embedded in non-cohesive soils. Wind Energy Science, 7(4), 1399–1419. doi:10.5194/wes-7-1399-2022.

[32] Rovere, M. (2004). Cyclic loading test machine for caisson suction foundations. Ecole Centrale de Lille/Politecnico di Milano, Milan, Italy.

[33] Abadie, C. (2015). Cyclic lateral loading of monopile foundations in cohesionless soils. Ph.D. Thesis, University of Oxford, Oxford, United Kingdom.

[34] Bolton, M. D. (1986). The strength and dilatancy of sands. Geotechnique, 36(1), 65–78. doi:10.1680/geot.1986.36.1.65.

[35] Garnier, J., Gaudin, C., Springman, S. M., Culligan, P. J., Goodings, D., Konig, D., Kutter, B., Phillips, R., Randolph, M. F., & Thorel, L. (2007). Catalogue of scaling laws and similitude questions in geotechnical centrifuge modelling. International Journal of Physical Modelling in Geotechnics, 7(3), 01–23. doi:10.1680/ijpmg.2007.070301.

[36] Manoliu, G., I1, D., V, D., Radulescu, N., & Dobrescu. (1984). International society for soil mechanics and foundation engineering. Geotextiles and Geomembranes, 1(2), 161–162. doi:10.1016/0266-1144(84)90012-8.

[37] Lee, J., Paik, K., Kim, D., & Park, D. (2012). Estimation of ultimate lateral load capacity of piles in sands using calibration chamber tests. Geotechnical Testing Journal, 35(4), 103756. doi:10.1520/GTJ103756.

[38] Frick, D., & Achmus, M. (2020). An experimental study on the parameters affecting the cyclic lateral response of monopiles for offshore wind turbines in sand. Soils and Foundations, 60(6), 1570–1587. doi:10.1016/j.sandf.2020.10.004.

[39] Jalbi, S., Arany, L., Salem, A. R., Cui, L., & Bhattacharya, S. (2019). A method to predict the cyclic loading profiles (one-way or two-way) for monopile supported offshore wind turbines. Marine Structures, 63, 65–83. doi:10.1016/j.marstruc.2018.09.002.